Fe-N-C in Proton Exchange Membrane Fuel Cells: Impact of Ionomer Loading on Degradation and Stability

Angus Pedersen, Rifael Snitkoff-Sol, Yan Presman, Laetitia Dubau, Rongsheng Cai, Jesús Barrio, Sarah Haigh, Frédéric Maillard, Ifan Stephens, Maria-Magdalena Titirici, et al.

ADVANCED ENERGY MATERIALS
www.advenergymat.de

Fe-N-C in Proton Exchange Membrane Fuel Cells: Impact of Ionomer Loading on Degradation and Stability

Angus Pedersen, Rifael Z. Snitkoff-Sol, Yan Presman, Laetitia Dubau, Rongsheng Cai, Jesús Barrio, Sarah J. Haigh, Frédéric Maillard, Ifan E. L. Stephens, Maria-Magdalena Titirici,* and Lior Elbaz**

Fe single atoms in N-doped C (Fe-N-C) present the most promising replacement for carbon-supported Pt-based catalysts for the O_2 reduction reaction at the cathode of proton exchange membrane fuel cells (PEMFCs). However, it remains unclear how the I/C ratio affects Fe-N-C degradation and the stability of single Fe atom active sites (FeN_x). Here, an accelerated stress test (AST) protocol is combined with emerging electrochemical techniques for a porous Fe-N-C in PEMFC with a range of I/C ratios. The PEMFC current density degradation rates are found to be comparable; however, with increased I/C ratio the additional FeN_x sites accessed are more stable, as shown by their higher active site stability number (electrons passed per FeN_x lost) at the end of the AST protocol. Meanwhile, the initial rate of TOF decay is suppressed with increasing I/C. Electrochemical process changes are studied via distribution of relaxation times analysis. Minor changes in H^+ and O_2 transport resistance at low current density prove kinetic degradation dominants at high potentials. These findings demonstrate how electrochemical techniques can be combined with stability metrics to determine and deconvolute changes from the active site to device level electrochemical processes in PEMFCs.

1. Introduction

Proton exchange membrane fuel cell's (PEMFC) performance is limited by ohmic, mass transfer and kinetic losses, with the later typically contributing the most significant loss due to the sluggish kinetics of the O_2 reduction reaction at the cathode.[1] This necessitates large quantities of Pt-based nanoparticle in current commercial PEMFC systems. Economic models of Pt-based cathodes in PEMFC stacks at significant production rates (500 000 stacks $year^{-1}$) predict the Pt catalyst would make up 26%–40% of the stack cost, depending on the Pt performance.[2,3] This highlights that the Pt content should be further reduced or completely eliminated to increase uptake of this green energy technology. In this regard, single metal atoms in N-doped C catalysts (M-N-C), in particular Fe-N-C, are found to be the most promising

A. Pedersen, I. E. L. Stephens
Department of Materials
Royal School of Mines
Imperial College London
London SW7 2AZ, England
E-mail: a.pedersen19@imperial.ac.uk

A. Pedersen, J. Barrio, M.-M. Titirici
Department of Chemical Engineering
Imperial College London
London SW7 2AZ, England
E-mail: m.titirici@imperial.ac.uk

A. Pedersen, R. Z. Snitkoff-Sol, Y. Presman, L. Elbaz
Institute of Nanotechnology and Advanced Materials and the Department of Chemistry
Bar-Ilan University
Ramat Gan 5290002, Israel
E-mail: lior.elbaz@biu.ac.il

The ORCID identification number(s) for the author(s) of this article can be found under https://doi.org/10.1002/aenm.202403920

DOI: 10.1002/aenm.202403920

L. Dubau, F. Maillard
Univ. Grenoble Alpes
Univ. Savoie-Mont-Blanc
CNRS
Grenoble-INP
LEPMI
Grenoble 38000, France

R. Cai, S. J. Haigh
Department of Materials
University of Manchester
Manchester M13 9PL, England

R. Cai
State Key Laboratory of Solid Lubrication
Lanzhou Institute of Chemical Physics
Chinese Academy of Sciences
Lanzhou 730000, China

M.-M. Titirici
Advanced Institute for Materials Research (WPI-AIMR)
Tohoku University
2-1-1 Katahira, Aobaku, Sendai, Miyagi 980–8577, Japan

replacement for Pt at the cathode of PEMFCs, which can present a cheaper, more accessible, and environmentally benign catalyst synthesis approach.[2,3]

Significant improvements in durability of Fe-N-C in PEMFCs have been achieved using catalysts made by depositing atomically thin N-C coatings, demonstrating PEMFC performance beyond 300 hrs under H_2/air supply at 0.67 V.[4,5] Additionally, Wu and coworkers reported that reductive pyrolysis (10% H_2/90% Ar) can reduce degradation over 200 h without comprising performance at 0.67 V.[5] Still, for practical transport applications such as light-duty vehicles, Fe-N-C has not approached the ultimate US Department of Energy (DoE) targets of 8000 h with <10% degradation at 0.3 A cm^{-2} and 0.8 V.[6]

The fast degradation of Fe-N-Cs in PEMFCs can be attributed to several factors,[7] which can be classified into indirect (support) and direct (active site) modifications of the N-doped C matrix. Support modifications includes protonation of N in FeN_x sites in ammonia-pyrolyzed Fe-N-Cs[8] and oxidation of the N-C support by hydroxyl and/or hydroperoxyl radicals derived from Fenton reaction between Fe cations and H_2O_2, reducing the turnover frequency of FeN_x active sites.[9–14] This degradation can be reduced by removal of Fe particles via acid washing during the synthesis.[15] *Operando* approaches measuring the concentration of H_2O_2 generated in Fe-N-C-based PEMFCs found the concentration reaching 17 mM,[16] with H_2O_2-related instability found to be linked to the amount of ORR charge passed.[17] Oxidation of carbon and increased hydrophilicity in Fe-N-Cs was proposed to lead to micropore flooding,[18,19] where FeN_x active sites have been proposed to be located;[20–24] however, experiments by Banham and coworkers concluded that micropore flooding does not contribute significantly to PEMFC performance decay for their studied Fe-N-C.[25] Meanwhile, carbon corrosion currents >0.1 mA cm^{-2} have been reported in Fe-N-C-based PEMFCs (at 80 °C) at ≥ 0.7 V, based on measurements under H_2-N_2.[17,26] In Pt/C, defective graphite crystallite domains of high surface area carbon supports preferentially oxidized between $0.80 < E < 1.00$ V_{RHE},[27] although the nature of the carbon support was found to play a minor role in the extent of Pt electrochemically active surface area loss in the potential range $0.60 < E < 1.0$ V_{RHE}.[28] Direct changes to active metal center in M-N-Cs can also occur, such as agglomeration and aggregation, in addition to demetallation and dissolution.[10,26,29,30]

Studies aimed at deconvoluting the contributions of different degradation mechanisms of Fe-N-Cs in acidic environments have found the mechanism and rate of degradation is highly dependent on the potential window in the accelerated stress test (AST),[31,32] temperature,[29,32] humidity,[32] and gas supply.[17,33] Considering gas supply, degradation rates in Fe-N-C follow O_2 > air >> N_2.[33–35] For instance, Osmieri et al. found increased rates of degradation under air-fed versus N_2-fed PEMFC Fe-N-C cathodes (AST: 3 s holds at 0.95 and 0.6 V, 80 °C), with no nanoparticle formation observed post-mortem.[34] Additionally, reduced Fe-N-C degradation has been reported under H_2/air than H_2/O_2.[35] To help standardize AST testing, Zelenay et al. established an AST protocol for M-N-Cs in PEMFCs.[36] However, prior to the AST, there is no ideal conditioning procedure for Fe-N-Cs since their electrochemical, chemical, and structural properties can be highly variable and can degrade rapidly, even from electrode manufacturing.[37]

After carrying out ASTs it is important to understand what the debilitating degradation mechanisms are and whether they relative to kinetics, mass transport or ohmic losses. Measuring the change in electrochemical active site density (EASD), and subsequently turnover frequency (TOF), is one direct method to understand kinetic changes at the active site level on Fe-N-C performance. Bae et al. found from *operando* Fe dissolution measurements of the zeolitic imidazolate framework (ZIF)-8-derived Fe-N-C in gas diffusion electrodes (GDE) (0.6 V_{RHE} at 80 °C, O_2/Ar) that the most significant changes in EASD occur within the first 30 min, followed by a continuous decrease in TOF up to 120 min.[38] Bae et al. also found that Fe-N-Cs synthesized with initially higher EASD displayed increased rates of FeN_x loss.[39] Due to the *operando* dissolution and reprecipitation of Fe species in acidic media owing to pH changes,[30] the FeN_x EASD cannot simply be determined from dissolved Fe content. Ex situ methods to probe the number of active sites exist, such as CO cryo sorption[40] and acid leaching;[41] however, their ex situ nature means their application to PEMFCs becomes challenging, especially when hot pressing is used for sample preparation. Instead, electrochemical approaches to measuring EASD are favorable, such as in situ nitrite stripping to track the change in FeN_x EASD.[42] However, this approach is limited as it is unable to selectively probe only single atom FeN_x active sites, instead also counting N-C micropores[43,44] and iron oxides.[33] Moreover, there are conflicting claims in the number of electrons transferred during the electrochemical stripping process (3 or 5 e^-).[42,45] Cyanide is another electrochemical probe technique;[46] but it suffers from safety concerns.

An alternative electrochemical method is to monitor the change over the AST of the reversible Fe^{2+}/Fe^{3+} redox couple at *ca* 0.76 V_{RHE}, which has been extensively confirmed as arising from surface confined FeN_x sites.[47–49] Microcavity measurements have also recently shown that Nafion is not responsible for FeN_x redox peaks.[50] The FeN_x sites providing the Fe redox have been previously assigned to active but unstable high spin $Fe^{3+}N_x$ sites.[48] Nevertheless, quantification based on direct integration of the Fe redox in cyclic voltammetry (CV) can be prone to inaccuracies due to the often minor Fe^{2+}/Fe^{3+} redox and its overlap with broad redox arising from quinone/hydroquinone species on the carbon surface.[51,52] Snitkoff-Sol et al. applied Fourier Transformed alternating current voltammetry (FTacV) to tackle these issues. In FTacV measurements, a large amplitude sinewave, superimposed on a dc potential ramp, is applied to the electrochemical system.[53] The resulting ac current undergoes signal processing to extract the harmonic components arising from non-linear responses in the system. The higher order harmonic components (fourth and above) are ideally devoid of more linear processes such as the double layer charging currents[54] and will mainly consist of the response of reversible/quasi-reversible redox reactions, such as the Fe^{2+}/Fe^{3+} redox couple arising from the FeN_x active sites. Therefore this signal can be used to accurately quantify the EASD.[55–59] Studying a commercial Fe-N-C (PMF-011904, Pajarito Powder LCC) under an AST in PEMFC (40 h hold at 0.6 V, H_2-O_2, 80 °C), they found a constant rate of EASD loss over time and a distinct change in TOF after 4 h.

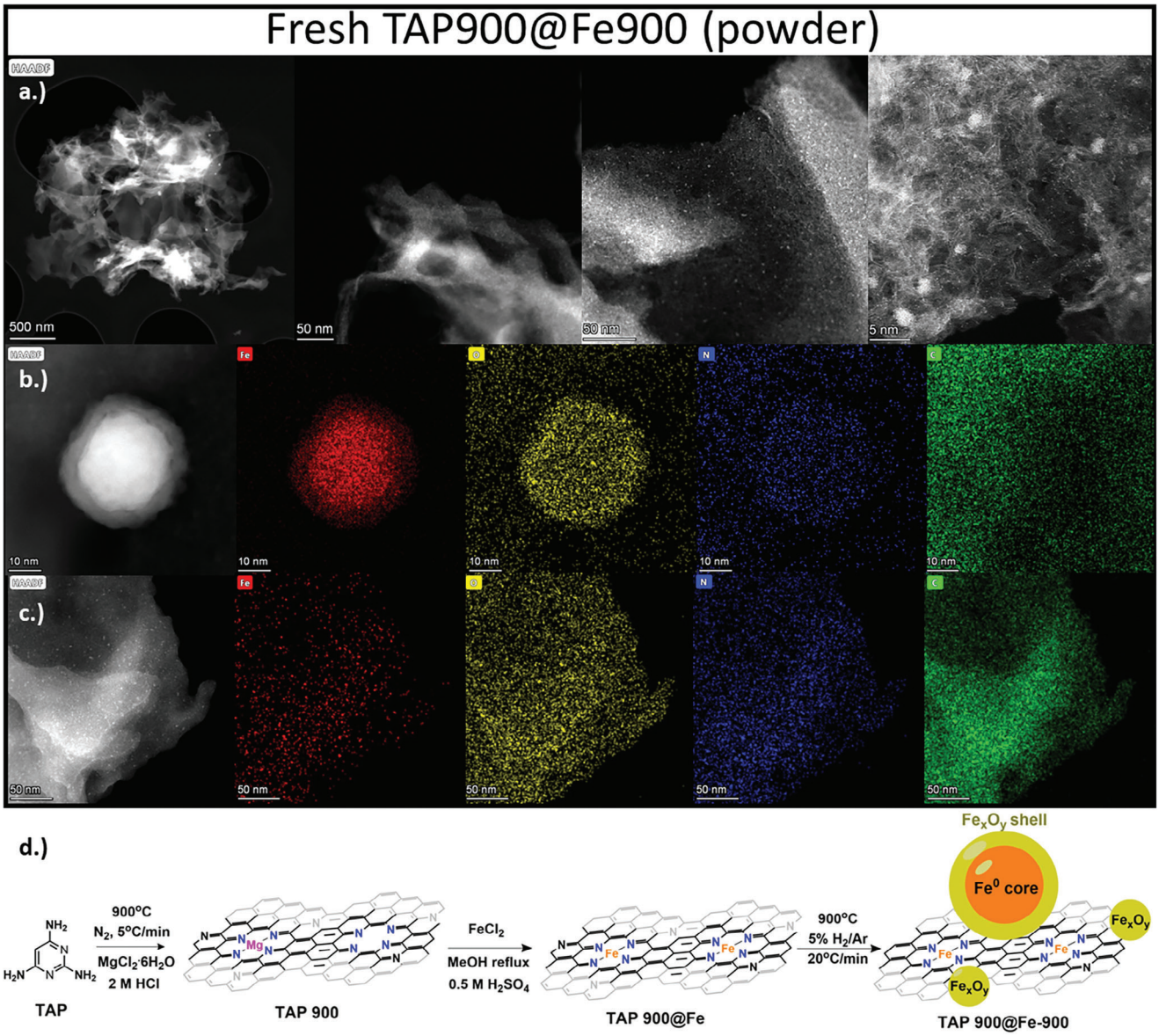

Figure 1. HAADF-STEM and STEM-EDXS elemental mapping of TAP 900@Fe900. a) HAADF-STEM images showing catalysts morphology at increasing magnification (left to right). b) HAADF-STEM and corresponding STEM-EDXS elemental maps for a representative particle of 40 nm diameter revealing a core shell structure. c) HAADF-STEM and corresponding STEM-EDXS elemental maps for a representative area of support without large Fe-rich particles. d) Simplified schematic representation of TAP 900@Fe900 metal sites over synthesis. The FeN_x and MgN_x sites could have axial ligands.[70]

Another important active site stability metric is the stability number (S-number), proposed by Geiger, Cherevko et al. as a simple and universal metric to determine the intrinsic stability of active sites, taking into account the amount of product produced, or charge passed, and number of active sites lost.[60] Thus, the S-number can be considered as an electrochemical turnover number and can be used to predict catalyst lifetimes,[60] although, to date, it been rarely applied in the O_2 reduction and M-N-C field,[61,62] partly due to difficulties in tracking EASD of M-N-C over ASTs.

Aside from probing the active site, changes in PEMFC performance can occur due to changes in proton and electron conductivity and O_2 diffusion over the AST. Liu et al. and Meyer et al. provided the first view of the impact of these different processes on Fe-N-C PEMFC performance over ASTs by extracting the distribution of relaxation times (DRT) from electrochemical impedance spectroscopy (EIS) measurements.[52,63] DRT analysis can deconvolute different electrochemical processes and quantify their contributions to kinetic, ohmic and mass transport losses from EIS, without the need for equivalent circuit fitting.[52,63–65]

As discussed above, there has been substantial work on deciphering the pathway and impact of M-N-C degradation mechanisms; however, the influence of the ionomer on the stability and degradation of M-N-Cs has remained unexplored. Banham et al. suggested that low equivalent weight ionomers improve Fe-N-C

stability in PEMFC due to their improved protonic conductance. This was hypothesized to be caused by the reaction zone progressing away from the membrane over the stability test, causing increased ohmic resistance.[35] Meanwhile, Jaouen and coworkers observed from *post-mortem* Fe and F energy dispersive X-ray spectroscopy (EDXS) elemental mapping in aged Fe-N-C cathodes in PEMFCs (50 h, H_2/O_2 at 0.5 V, 80 °C) that Fe clustering was linked to the presence of Nafion ionomer, with high spin $Fe^{3+}N_x$ sites rapidly forming Fe_xO_y sites.[48] In addition, FeN_x active sites have been reported to predominantly reside within micropores,[20–24] which is typically expected to be inaccessible to direct Nafion micelle contact.

The dissolution of Fe species accelerates Fenton's reactions with H_2O_2, creating hydroxyl radicals that attack the membrane and ionomer, with Fe species also partially exchanging with protons in the ionomer.[66–68] Although, the oxidation of the carbon surface by H_2O_2-derived radicals has been suggested to help evenly distribute ionomer over the Fe-N-C surface and cause favorable ionomer side-chain interactions.[69]

We previously synthesized a hierarchical highly porous and high FeN_x utilization Fe-N-C,[70] reporting on the significant Fe dissolution on degradation in acid,[30] and the impact of ionomer to Fe-N-C ($0.7 \leq I/C \leq 4.9$) ratio on initial PEMFC performance.[71] Building on these works, here we investigate the impact of the I/C ($2.1 \leq I/C \leq 4.9$) on this highly porous Fe-N-C's stability and PEMFC degradation.[71] We focus on $I/C \geq 2.1$, since lower I/C gave poor initial PEMFC performance (<50 mA cm^{-2} at 0.75 V). Degradation monitoring was achieved by using a combination of initial and *post-mortem* characterization (Raman spectroscopy, microscopy, and EDXS) and electrochemical techniques (CV, FTacV, and DRT).

2. Results and Discussion

2.1. Catalyst Powder Characterization

Following synthesis of TAP 900@Fe900, the highly porous catalyst was previously characterized by N_2 sorption, X-ray diffraction, SEM, and low magnification HAADF-STEM.[71] Here, HAADF-STEM at higher magnification Z-contrast images (rightmost images in **Figures** 1a and S2a, Supporting Information) show curved line features, suggesting the support consists of disordered atomic planes. The spacing between the curved planes was consistent with graphite (002) basal plane spacing (≈0.34 nm, Figure S2a, Supporting Information); however, these were only present in nm-sized regions. Meanwhile, some areas under HAADF-STEM displayed 0.8 nm lattice spacing (Figure S2a, Supporting Information), suggesting the carbon layers were fully exfoliated. This is consistent with previous XRD measurements of TAP 900@Fe900, which did not show a distinct graphite (002) peak due to their nm-sized domains.[71] Brighter features are also visible across TAP 900@Fe900, showing a distribution of both atomic metal species and small metal-rich clusters (< 5 nm), as well as larger metal particles (≈40 nm) in some regions. Previous characterization of pristine TAP 900@Fe (before the second reductive pyrolysis) found no presence of small or large Fe particles within TAP 900@Fe, due to the decoupled initial pyrolysis and subsequent low temperature Fe (trans-)metalation approach, which was followed by acid washing.[70] Therefore, the appearance of Fe particles in TAP 900@Fe900 is related to the second reductive pyrolysis step here, where acid washing did not follow.

EDXS elemental mapping on the 40 nm diameter metallic particles (Figures 1b and S2b, Supporting Information) show a core-shell structure with an Fe core (30 nm diameter) and Fe_xO_y shell (5 nm radius), with high magnification HAADF STEM images showing these shells are crystalline. Similar Fe/Fe_xO_y core/shell nanoparticles have been reported under reductive pyrolysis of iron(II) acetate (20% H_2/N_2, 800 °C).[72] STEM-EDXS analysis showed that the metal containing nanoclusters (<5 nm) contained both Fe and O, so these are proposed to be Fe_xO_y (Figure 1c). This species can spontaneously form when nanosized Fe species are in contact with air,[73] which could occur from trace O_2 present in the furnace during "pyrolysis", or from the final 80 °C drying step in air, before samples were stored in a N_2. Figure 1d depicts the proposed structures present at different stages during the synthesis process. STEM-EDXS elemental mapping also show Si contamination, as well as Cl and S (Figure S2b–d, Supporting Information), coming from the $FeCl_2$ precursor (Cl), glassware (Si) and acid washing steps in 2 M HCl and 0.5 M H_2SO_4 (Cl and S).

2.2. PEMFC Measurements

TAP 900@Fe900 powders were fabricated into electrodes with I/C = 2.1, 3.5, 4.2 and 4.9 and tested in a PEMFC (Experimental Section) according to the AST protocol outlined in Table S1 and Figure S1 (Supporting Information). The PEMFC cathodic polarization curves for TAP 900@Fe900 at I/C = 2.1, 3.5, 4.2 and 4.9 over the AST protocol (Figure S1 and Table S1, Supporting Information) are presented in **Figure** 2a–d with high frequency resistance-free (HFR)-free results in Figure S3a–d (Supporting Information). For comparison the geometric current density (i_{geo}) at 0.75 V and 0.75 $V_{HFR\text{-}free}$ is shown in Figures 2e and S3e (Supporting Information), respectively. The initial PEMFC performance for varying I/C was thoroughly discussed in our previous work,[71] therefore we focus on subsequent protocol measurements and trends. After the initial polarization curve, PEMFCs were held at 0.4 V under H_2-O_2 for a 20 min "break-in" procedure (Figure S4, Supporting Information). At I/C = 2.1, there is no distinct change in current density at 0.4 V, while the HFR values fell from 943 to 835 mΩ cm^2 over the 20 min hold. Meanwhile, at I/C ratios ≥3.5, there is initially higher current density, indicative of more EASD, with significant degradation over this short period. For instance, at I/C = 3.5 and 4.9 the i_{geo} at 0.4 V fell from 516 to 383 mA cm^{-2} and from 404 to 298 mA cm^{-2}, respectively. HFR values only fell minorly for all I/C ratios, in the range 371–285 mΩ cm^2. The persistently and relatively high HFR values are likely a result of low through plane electronic conductivity of the TAP 900@Fe900 layer,[71,74] with some contribution from the thick (50 µm) Nafion N212 membrane. After the 20 min hold at 0.4 V, the least significant drop in i_{geo} at 0.75 V occurred for I/C = 2.1 (Figure 2a,e). After the 20 min hold at 0.4 V, there is no significant change in HFR over the AST cycling for all I/C ratios (Figure S5, Supporting Information). In the case of I/C = 4.9, HFR remained constant over the AST protocol, which is speculated to be due to over-saturation of ionomer. Correcting for HFR

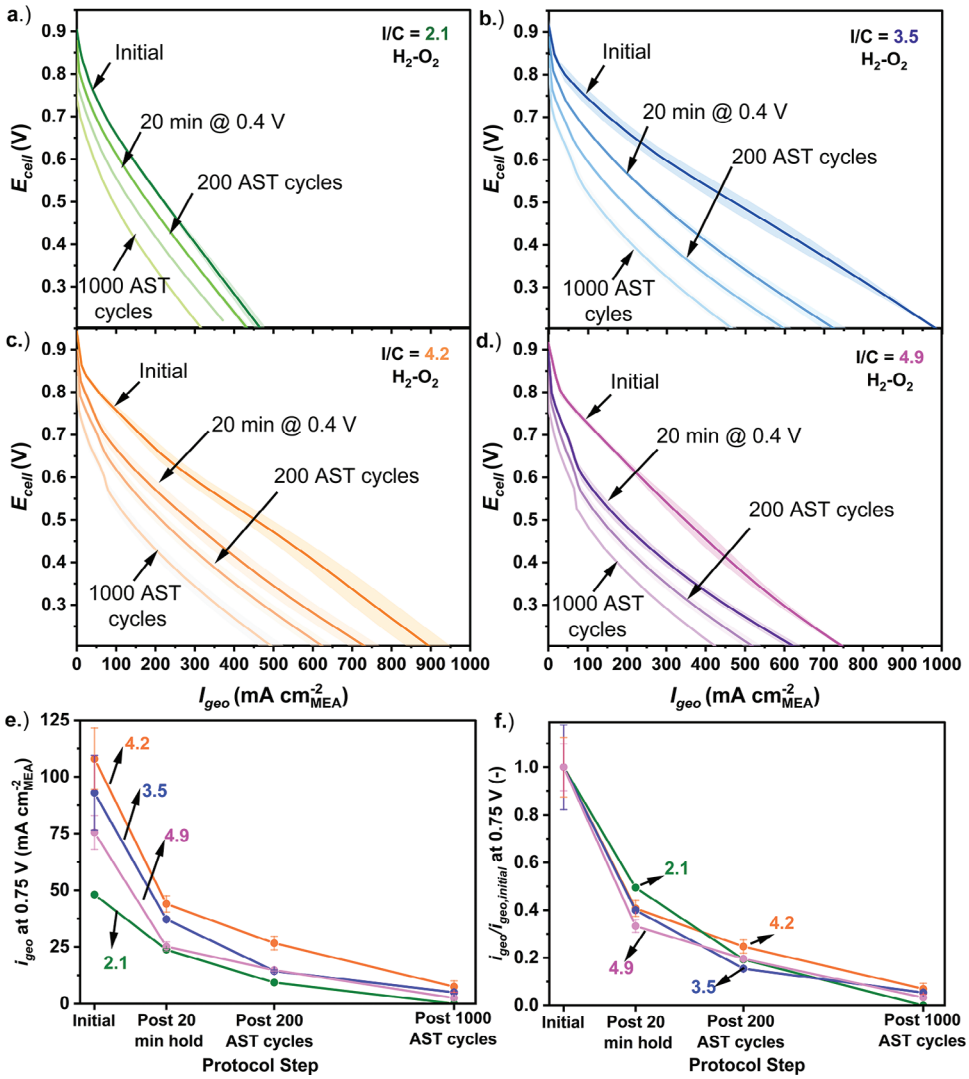

Figure 2. H_2-O_2 (0.7/1.7 SLPM flow rate) PEMFC polarization cathodic scan (50 mV steps) at 1 bar_g back pressure and 80 °C over accelerated stress test (AST) protocol for I/C = a) 2.1. b) 3.5. c) 4.2. d.) 4.9. e) Geometric current density and f) Normalized geometric current density at 0.75 V over AST cycels. Cathode loadings: 1.35 ± 0.03 $mg_{Fe\text{-}N\text{-}C}$ cm^{-2} on Sigracet BC29. Anode: 0.2 mg_{Pt} cm^{-2} on Sigracet 22BB, with Nafion® 212 membrane and 1 cm^2_{geo} active area. Average of two results shown with shaded regions or error bars representing error.

(Equation (5)), the PEMFC performance of I/C = 2.1 falls in line with the top performing I/C results after the 20 min hold at 0.4 V (Figure S3e, Supporting Information).

Next, the 200 and then 800 AST cycles were carried out, consisting of repeated 3 s holds at 0.9 and 0.6 V under H_2-O_2. It should be noted that in the protocol, galvanic EIS (at 50 and 100 mA cm^{-2}) was carried out in between AST stages, thus also contributing to degradation (Figure S1 and Table S1, Supporting Information). Again, significant degradation in PEMFC i_{geo} occurred for TAP 900@Fe900 at all I/C ratios, approaching or reaching 0 mA cm^{-2} at 0.75 V after the 1000 AST cycles (Figure 2e). I/C = 4.2 maintained the greatest i_{geo} at 0.75 V in the polarization curve throughout the whole AST protocol, with 11 mA cm^{-2} remaining after 1000 AST cycles (Figure 2e). Tafel plots are shown in Figure S6 (Supporting Information) for comparison of performance PEMFC changes occurring over the AST within the kinetic region of the polarization curve. The shift to lower voltages within the low-medium current region of the polarization curves at different stages in the AST protocol indicates significant kinetic degradation.

For relative comparison, the normalized performance ($i_{geo}/i_{geo,\ initial}$) at 0.75 V and 0.75 $V_{HFR\text{-}free}$ is shown in Figure 2f and Figure S3f (Supporting Information), respectively. There are not notable differences in the relative decreases in the normalized current density across the range of I/C tested. However, this plot does not consider the changes at the active site level and the amount of charge passed over the AST (Table S2, Supporting Information), which varies for the I/C ratios due to their different PEMFC performance. Therefore, to delve deeper and understand changes at the active site level, active site stability metrics need to be considered, as discussed later.

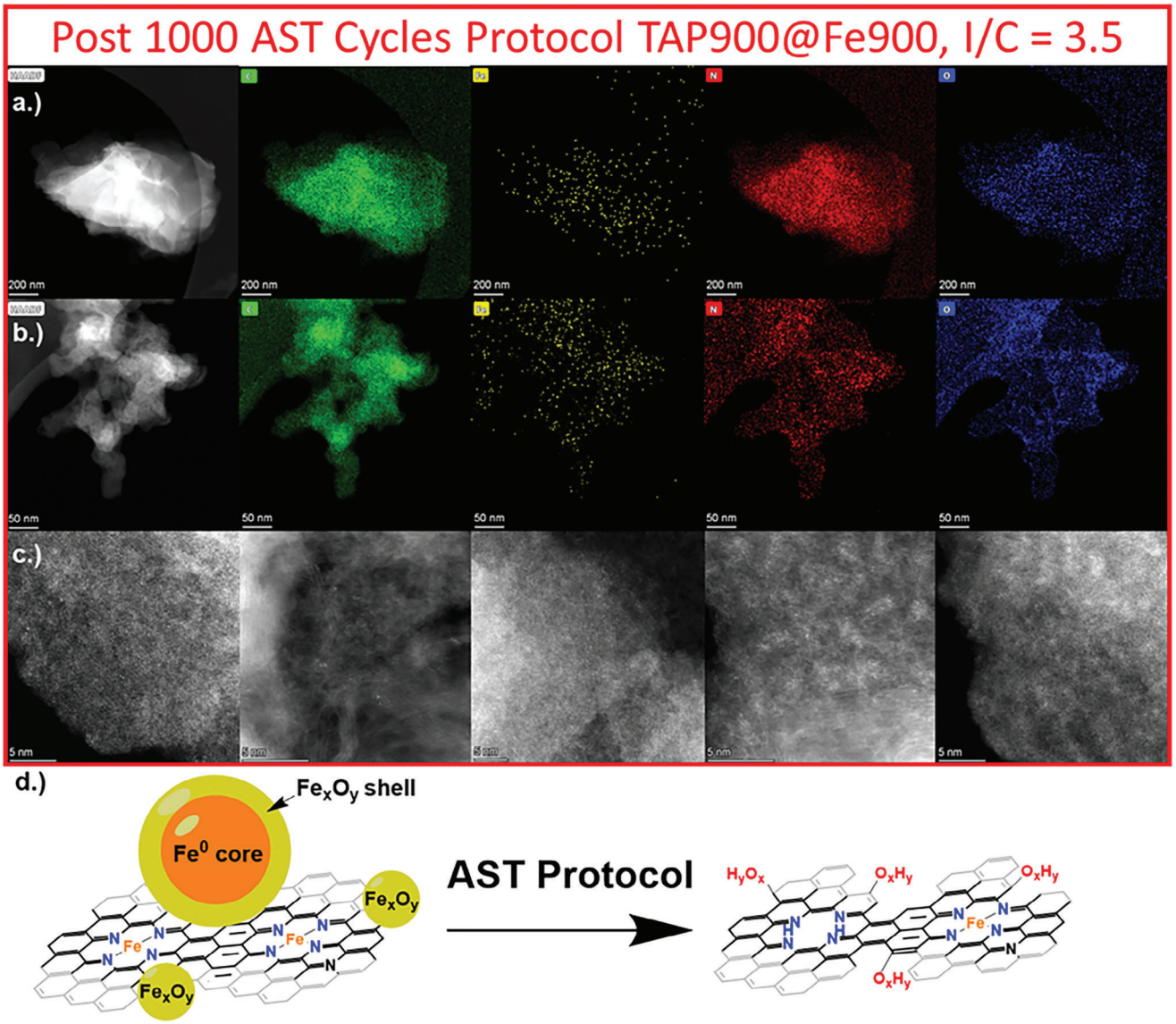

Figure 3. HAADF-STEM and EDXS elemental maps of TAP 900@Fe900 post 1000 AST cycles at I/C = 3.5 with a) 200 nm scale bar and b) 50 nm scale bar. c) representative HAADF-STEM images at higher magnification (5 nm scale bar). d) Simplified schematic representing the changes occurring at the active site level and with Fe species over the AST protocol.

The rapid degradation of TAP900@Fe900 under O_2 supply in PEMFC (80 °C) is analogous to that of TAP900@Fe in GDE at 75 °C under O_2.[30] This indicates the reductive pyrolysis (5% H_2/95% Ar) of TAP 900@Fe did not result in any significant enhancement of durability. This is different to the recent report of Wu and coworkers who reported a substantial improvement for the ZIF-8-derived Fe-N-C following reductive pyrolysis (10% H_2/90% Ar).[5] To understand these differences, post-mortem characterization is required.

2.3. Post-Mortem Characterization

Following PEMFC AST measurements, the membrane electrode assemblies were characterized. Contrary to the *post-mortem* report of Jaouen and coworkers, Fe-N-C in PEMFC (AST: 50 h at 0.5 V, H_2-O_2),[48] we do not observe clustering of Fe$_x$O$_y$ particles from *post-mortem* microscopy of the TAP 900@Fe900 particles (**Figures 3** and S7, Supporting Information). Instead, at I/C = 3.5, according to HAADF-STEM and EDXS, we see the near-complete removal of Fe particles and clusters from the catalyst layer, with only atomically dispersed Fe atoms remaining (Figures 3c and S7b, Supporting Information). The removal of large Fe particles and the reduced Fe concentration is further supported by comparison of SEM, TEM and EDXS before and after 1000 AST cycle protocol at I/C = 3.5 and 4.9 (Figures S8–S11, Supporting Information). Evaluating the TEM-EDXS composition based on Fe and C (Figure S12, Supporting Information), the Fe concentration falls from 0.19 ± 0.04 at.% in the fresh TAP 900@Fe900 electrode to 0.05 ± 0.04 at.% (I/C = 3.5) and 0.06 ± 0.05 at.% (I/C

= 4.9) after the 1000 AST protocol. Only very rare sightings of Fe particles, which appear encapsulated, were found *post-mortem* (Figure S10b, Supporting Information), likely arising from Fe impurities from the N-C precursor (TAP = 97% pure). Therefore, the removal of Fe particles appears independent of the I/C range considered. SEM and TEM also indicate no obvious changes in catalyst pore structure or graphitization after the 1000 AST protocol (Figures S8–S11, Supporting Information) for any I/C ratio, but slight delamination at the membrane-TAP 900@Fe900 interface appeared (Figures S8b and S9b, Supporting Information).

Our previous measurements of TAP 900@Fe in gas diffusion electrodes also found no observable Fe particles after a 200 cycles of the AST protocol (3 s holds at 0.9 and 0.6 $V_{RHE,\ iR\text{-}free}$) under O_2 at 75 °C, but Fe particles were observed at 20 °C, due to local pH changes.[30] The lack of Fe particles observed *post-mortem* here matches the report of Osmieri et al. who conducted a similar AST protocol to our work (AST: 3 s holds at 0.95 and 0.6 V, H_2-O_2, 80 °C).[34] This suggests the conditions used in the AST (temperature, potentials applied and current drawn) highly impacts *post-mortem* observations. The different observations could also be attributed to the vastly different catalyst morphology and porosity, where TAP 900@Fe900 exhibits an accessible structure with hierarchal porosity, which facilitates rapid transport of Fe cations out of the Fe-N-C particles and layer. Meanwhile Jaouen and coworkers ZIF-8 derived Fe-N-C is microporous and bulky,[48] which would restrict Fe cation diffusion, possible explaining their observations of Fe clustering in certain areas of the electrode after their AST protocol.

In interpreting the Raman spectra from TAP 900@Fe900 pre and post 1000 AST protocol (Figure S13, Supporting Information), the focus is placed only on the variations in intensity/shape of the bands due to uncertainty associated with the deconvolution of the Raman spectra for disordered high surface area carbon supports. The G-band (≈1585 cm^{-1}) is assigned to the quasi-graphitic crystallites, while the *D*1-band (≈1340 cm^{-1}) is assigned to the edge-defects on these crystallites.[28] The *D*2-band (≈1610 cm^{-1}) is assigned to defects present in the surface of graphite crystallites. *D*3 (≈1495 cm^{-1}) is assigned to amorphous carbon.[28] Comparing the Raman spectroscopy of the pristine TAP 900@Fe900 powder to post 1000 AST protocol electrodes with I/C = 2.1 and 4.2 (Figure S13, Supporting Information), one can see a relative decrease in intensity of the *D*1, *D*2 and *D*3-bands. This suggests that corrosion of disordered graphitic lattices and amorphous carbon occurs over the relatively short 1000 AST protocol, with quasi-graphitic lattices (G-band) being preserved. The preferential oxidation of crystallite edges from the 1000 AST protocol is supported by the oxygen EDXS elemental mapping in Figure 3b. The corrosion and oxidations follows the observations of Castanheira et al., who found amorphous carbon and defective graphite crystallites were preferentially oxidized between $0.80 < E < 1.0$ V.[27] Based on the above characterization, the changes occurring within the catalyst at the active site level over the AST protocol are represented by Figure 3d.

2.4. Active Site Stability Metrics

To determine the impact of kinetic losses, deconvolution of active sites metrics is critical. In this regard we monitor the EASD by integration of the Fe^{3+}/Fe^{2+} redox in CV over the AST cycles for I/C = 2.1, 3.5, 4.2 and 4.9 (Figure S14, Supporting Information, Equation (1) and Equation (2)) with extracted $EASD_{CV}$ shown in **Figure 4a**. For simplicity we focus our analysis on redox active FeN_x sites. Assuming non-redox active FeN_x contribute to the PEMFC performance, the calculated EASD here will be underestimated and therefore the TOF and S-number will be overestimated.

Over the AST, broad quinone/hydroquinone redox become convoluted with the Fe^{3+}/Fe^{2+} redox (Figure S13, Supporting Information), causing some error during direct integration of the Fe redox in the CV. There is also a large error in the SD_{CV} of I/C = 2.1 due to the small Fe^{3+}/Fe^{2+} redox peak, resulting in a sizeable error in TOF_{CV} and S-$number_{CV}$. The precision of FTacV in isolating and accurately quantifying the Fe redox is therefore required. $EASD_{FTacV}$ is calculated from FTacV simulation results (Figure S15 and Table S3, Supporting Information). Meanwhile for I/C = 3.5 and 4.2, the values and trends for the active site metrics are very comparable between CV and FTacV, due to their large Fe^{3+}/Fe^{2+} redox. It is highlighted that the experimental FTacV data at I/C = 4.9 was poor, possibly due to the low electronic conductivity at this high I/C ratio. At this I/C, the poor FTacV data caused the extracted $EASD_{FTacV}$ values to be significantly underestimated (Figure S15d and Table S3, Supporting Information), therefore the S-$number_{FTacV}$ and TOF_{FTacV} would be overestimated. As a result, to avoid confusion this artificial data is not plotted.

As previously reported, increasing I/C increases the initial EASD, up to I/C 4.2 (Figures 4a and S16a, Supporting Information).[71] Regarding normalized $EASD_{CV}$ and $EASD_{FTacV}$ change over the AST protocol, it is observed that the rate of loss of EASD increases over the first 200 AST when changing from I/C = 2.1 to I/C ≥ 3.5 (Figures 4b and S16b, Supporting Information). The faster initial loss of FeN_x sites with increased initial EASD is analogous to the observations of Bae et al., who found their Fe-N-Cs synthesized with higher initial EASD lost their FeN_x sites at a faster rate.[39] The rate of loss of EASD are then more comparable over the next 800 AST cycles. In separate work, Bae et al. found 36% and 41% loss of FeN_x based on in situ nitrite stripping (3 electron process assumed) and ICP-MS, respectively, following 2 h hold at 0.6 V_{RHE} under O_2 for the ZIF-8-derived Fe-N-C. Here, the losses in $EASD_{CV}$ after the 1000 AST cycles (equivalent to ≈2 h under H_2-O_2, including GEIS) equate to 42% and 66% loss for I/C = 2.1 and 4.9, respectively (Figure 4b).

The loss in EASD does not consider the amount of charge passed during the AST protocol (Table S2, Supporting Information), which was substantially different for the I/C ratios due to their different PEMFC performance (Figure 2). The S-number is a simple metric which can resolve this issue by accounting for the charge passed and the loss in active sites (Equation (4)). A trend of decreasing S-$number_{CV}$ with increasing I/C is observed after 200 AST cycles (Figure 4c); however, no clear trend is observed for S-$number_{FTacV}$ at that AST interval for $2.1 \leq I/C \leq 4.2$ (Figure S16c, Supporting Information). Considering the normalized S-$number_{CV}$ and S-$number_{FTacV}$ (Figures 4d and S16d, Supporting Information), a common trend in I/C is observed after 1000 AST cycles, whereby the S-number increases with increasing I/C. This suggests the ionomer has a minor positive effect in stabilizing the FeN_x sites, perhaps due to improved maintenance

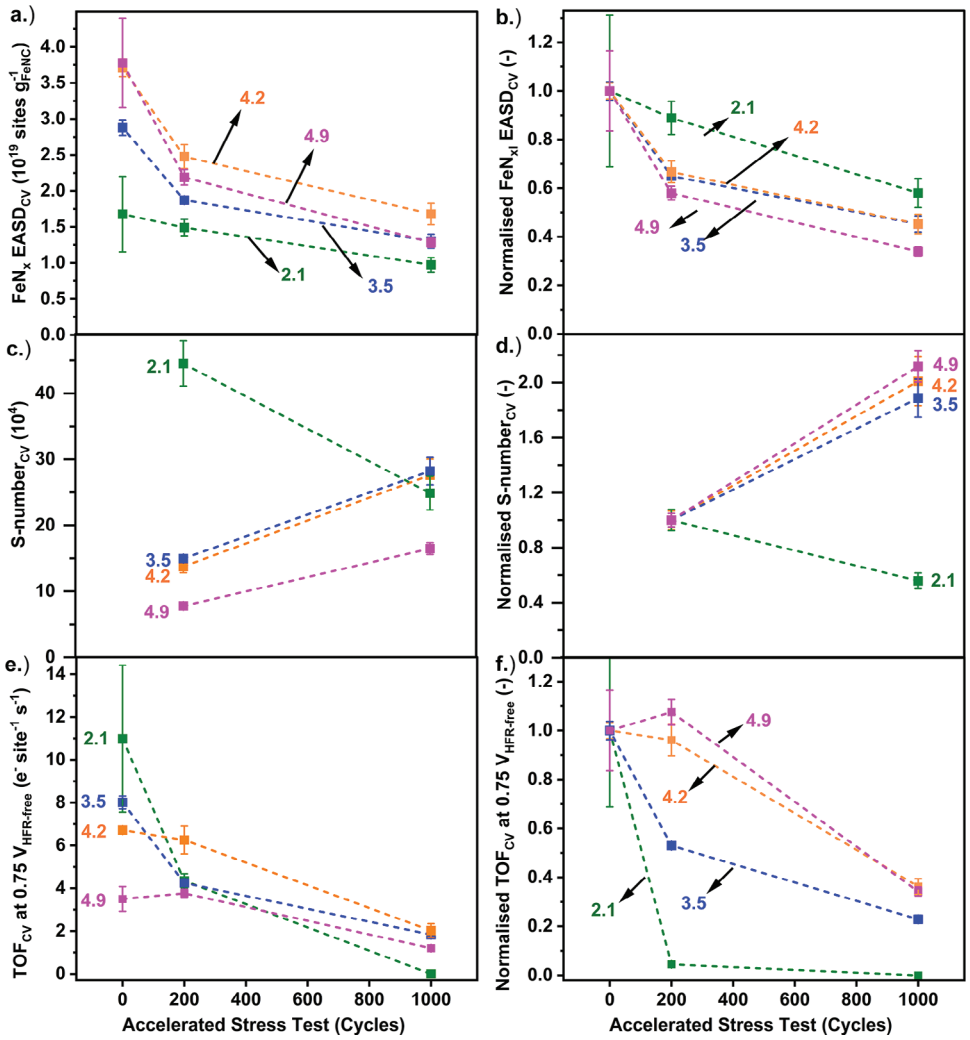

Figure 4. Change over the AST cycles of TAP 900@Fe900 in PEMFC for I/C = 2.1, 3.5, 4.2 and 4.9 in CV-derived metrics of a) $EASD_{CV}$. b) Normalized EASD. c) S-$number_{CV}$. d) Normalized S-$number_{CV}$. e) TOF_{CV} at 0.75 $V_{HFR\text{-}free}$. f) Normalized TOF_{CV} at 0.75 $V_{HFRfree}$. Data were normalized to their initial values. Error bars represent difference of EASD from integration of anode and cathode scan of Fe^{3+}/Fe^{2+} redox (under H_2-N_2 supply at 0.3 SLPM flowrate with 1 bar_g back pressure, Figure S12, Supporting Information).

of local pH. From previous *operando* dissolution measurements of TAP 900@Fe in gas diffusion electrodes we measured significant dissolved Fe concentrations (≈200 $ng_{Fe}\ g_{FeNC}^{-1}\ s^{-1}$) under O_2 at 75 °C at 0.9 $V_{RHE,\ iR\text{-}free}$ over 200 AST cycles (3 s holds at 0.9 and 0.6 $V_{RHE,\ iR\text{-}free}$).[30] This suggests Fe dissolution is likely the prominent mechanism of active site loss in TAP 900@ Fe900. Over the AST, the increased ionomer coverage with increasing I/C may help maintain an acidic local pH, preventing the Fe dissolution and subsequent formation of Fe_xO_y.[30]

Our previous calculations determined that a stability number of ≈10^8 would be required to reach the ultimate US DOE PEMFC target of 8000 h (with <10% degradation) at 0.3 A cm^{-2} and 0.8 V[6] (75 A $g_{M\text{-}N\text{-}C}^{-1}$ based on 4 $mg_{M\text{-}N\text{-}C}\ cm^{-2}$ and 1 × 10^{20} sites $g_{M\text{-}N\text{-}C}^{-1}$, assuming 1 AST cycle = 6 s, Figure S17, Supporting Information).[61] It should be considered that degradation and therefore the S-number is highly dependent on measurement conditions (e.g., cycling versus potential hold, the specific potentials, temperature and pH), preconditioning and measurement time. Nevertheless, for comparison, alkaline GDE measurements (at room temperature) by Ku et al. found the stability number changing from ≈10^6 to ≈10^7 for a commercial Fe-N-C (PMF-011904, Pajarito Powder LLC), when evaluating after 200 and 2000 AST cycles (3 s holds at 1 and 0.57 $V_{iR\text{-}free,\ RHE}$, equivalent to 0 to −125 mA cm^{-2}), respectively (Figure S17, Supporting Information).[62] Meanwhile, TAP 900@Fe900 after 1000 AST cycles protocol only shows an S-number ≈10^5 (Figure 4c), signifying the intrinsically low stability of the redox active FeN_x sites in TAP 900@Fe900.

After determining the EASD the TOF can also then be calculated (Equation (3)). Considering the TOF_{CV} and TOF_{FTacV} at 0.75 $V_{HFR\text{-}free}$ (Figures 4e,f and S16e,f, Supporting Information), another common trend is observed. I/C = 2.1 initially presents the highest TOF and I/C = 4.9 the lowest TOF. The TOF then decreases most rapidly during the first 200 AST cycles for I/C = 2.1 (e.g., TOF_{CV} 3 × 10^{-2} e^- $site^{-1}$ s^{-1} per cycle) with this rate of TOF_{CV} decay decreasing as I/C increases, with the TOF

increasing at I/C = 4.9 after 200 AST cycles. Between 200–1000 AST cycles the rate of TOF decay then reduces for I/C = 2.1 and 3.5 but increases for I/C = 4.2 and 4.9 (Figures 4e,f and S16e,f, Supporting Information). I/C = 2.1 displays a TOF_{CV} of complete loss activity after 1000 AST cycles, but 0.97×10^{19} sites g_{FeNC}^{-1} remain, suggesting several possible scenarios, which could occur separately or in tandem:

i.) Redox active FeN_x sites were deactivated by local carbon oxidation.

For all I/C ratios, broad quinone/hydroquinone redox in the CVs are observed (≈0.3–0.7 V) to evolve and increase over the AST protocol, mostly within the first 200 AST cycles (Figure S12, Supporting Information). *Post-mortem* Raman spectroscopy (Figure S13, Supporting Information) and oxygen EDXS elemental mapping (Figure 3b) provides evidence carbon oxidation and increased oxygen groups. The increase of these carbon-oxygen functionalities suggests oxidation of the carbon support via H_2O_2-derived radicals, where carbon oxidation local to the active site has been shown to decrease TOF,[14] and also to an increase in the hydrophilicity and therefore change in water management and transport properties.[75]

As the number of cycles increases so does the impact of Fenton reaction derived radicals from H_2O_2 on the TOF of FeN_x active sites,[14,38] with Fe-N-C based PEMFCs containing high concentrations of H_2O_2.[16] Additionally, H_2O_2-related instability was previously found to be related to the ORR charge.[17] Due to the dissolution of Fe particles (Figures 3 and S3, Supporting Information), Fenton reactions would be accelerated. Greater amounts of Nafion with increased I/C means more dissolved Fe species can partially exchange with H^+ in the ionomer[66–68] and therefore H^+ transport would be inhibited. O_2 transport in the ionomer has also been shown to be impeded when dosed with metal cations.[76]

ii.) There are two (or more) distinct types of redox active FeN_x present, with different TOF and stability.

Redox active FeN_x will possess a distribution of TOFs due to their dispersion within the heterogeneous carbon support.[55] Still, two distinct FeN_x active sites have been previously proposed, one site being more active but less stable and another site being loss active but more stable.[48] The former FeN_x site was found to undergo redox transitions, while the latter not.[48] Additionally, Snitkoff-Sol et al. reported two distinct TOF regimes over their AST (40 h hold at 0.6 V, H_2-O_2, 80 °C) for a commercial Fe-N-C (PMF-0144901, Pajarito Powder).[55]

Next, we carried out electrochemical impedance spectroscopy measurements under H_2-N_2 and H_2-O_2 (50 and 100 mA cm^{-2}) over the AST protocol (Figures S18–S21, Supporting Information). Subsequent DRT analysis then deconvoluted the H^+ and O_2 transport resistance (Figure S22, Supporting Information) to determine mass transport losses. The peaks appearing in the DRT plots were assigned to processes of: O_2 diffusion (0.1-2 Hz), ORR (2–200 Hz), H^+ in the catalyst layer (200–2000 Hz) and membrane (2000–15 000 Hz), based on previous works on Fe-N-Cs in PEMFC.[52,63,71] Over the AST protocol at I/C = 2.1, two H^+ catalyst layer transport peaks begin to appear (Figure S22a,b, Supporting Information), which we tentatively assign to the lower Nafion content in the bulk of the catalyst layer and higher Nafion concentration near the membrane. Fe dissolution causes degradation of the ionomer,[66–68] which is more pronounced at low I/C since there is less ionomer available. This Nafion variation is due to the additional 0.2 mg cm^{-2} Nafion sprayed on the surface of all TAP 900@Fe900 electrodes prior to hot-pressing (Experimental Section), therefore the Nafion variation would be most pronounced at I/C = 2.1. We do not consider contribution of the anode to the DRT based on the operating conditions and anode loading and previous works.[52,63,77] The resistance to these processes was then extracted based on integration of the peaks, resulting in **Figures 5** and S23 (Supporting Information). To note, the DRT resistance results prior to AST cycling were discussed in our previous work,[71] therefore here we focus on trends over the AST protocol. In theory there should be a trend and a correlation between the frequencies and the peak area as the frequency is related to the process kinetics; however, this scenario is not observed here.

At 50 and 100 mA cm^{-2} (H_2-O_2), the H^+ transport resistance in the catalyst layer at I/C = 2.1 constantly and significantly increases over 200 and 1000 AST cycles (Figures 5a and S23a, Supporting Information). This can be explained by the insufficient ionomer content at I/C = 2.1 and the primary O_2 reduction reaction shifting over the AST protocol in TAP 900@Fe900, where the reaction zone moves away from the membrane and thus H^+ supply. This scenario was proposed by Banham et al.[35] who also found the ionic conductance decreased with increasing ionomer equivalent weight, with 1100 equivalent weight (as used here) showing the lowest ionic conductance. Meanwhile, only minor changes in the catalyst layer H^+ transport resistance are observed for I/C ≥ 3.5, suggesting the ionomer content and conductance is sufficient at these I/C ratios over the AST protocol.

We reported on the apparent increase in the resistance of H^+ through the membrane with increasing I/C prior to AST cycling (Figures 5b and S23b, Supporting Information) in our previous publication.[71] In summary, we reasoned that the DRT peak assigned to the membrane consisted of the H^+ resistance of both the membrane and the membrane-TAP900@Fe900 interface, where an additional layer (0.2 mg cm^{-2}) of Nafion was sprayed before hot-pressing. The top layer of Nafion would infiltrate further into the TAP 900Fe900 at low I/C, leading to a greater H^+ resistance observed from the DRT membrane peak (Figures 5b and S23b, Supporting Information). The H^+ membrane resistance increased over the AST protocol for all I/C except 4.2 (Figures 5b and S23b, Supporting Information), which can be due to membrane degradation arising from significant and continuous dissolution of Fe from particles and FeN_x sites in TAP 900@Fe900. The Fe cations can exchange with protons in the ionomer and sulfonic acid groups of the membrane, reducing their H^+ conduction.[66–68] Fe dissolution over the AST protocol is supported by the fall in EASD (Figures 5b and S21b, Supporting Information) and Fe concentration from TEM-EDXS (Figure S12, Supporting Information).

The decreasing O_2 diffusion resistance at 50 and 100 mA cm^{-2} over the AST protocol for all I/C except I/C = 4.2 at 100 mA cm^{-2} (Figures 5c and S23c, Supporting Information) could be due to a favorable redistribution of ionomer from carbon oxidation of the Fe-N-C.[69] or the Nafion becoming more hydrated, thus

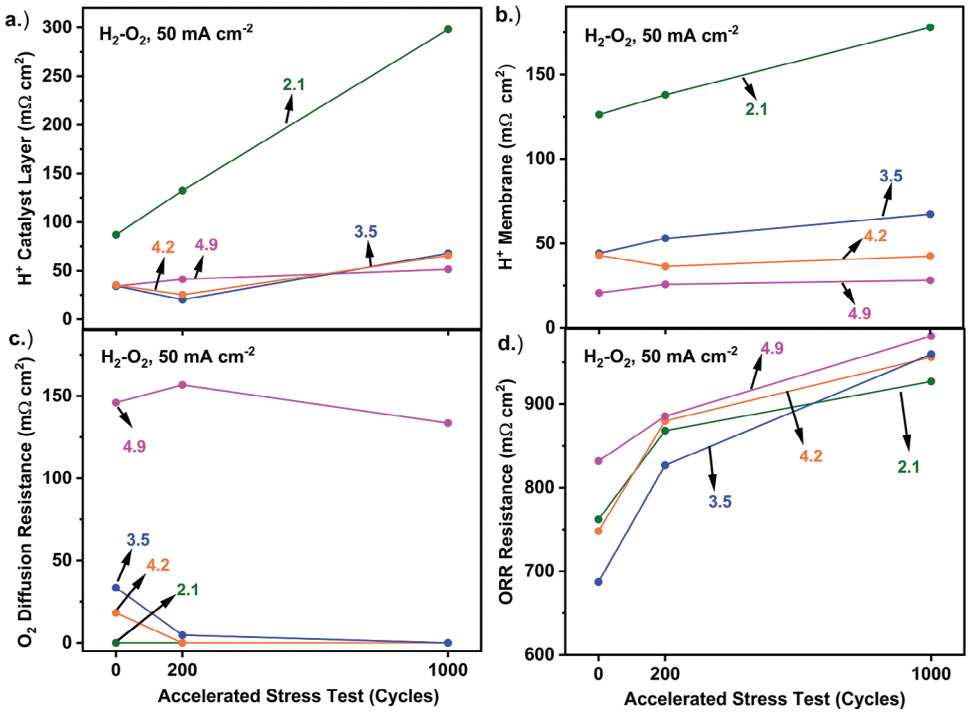

Figure 5. DRT results on PEMFC at varying I/C ratios for H_2-O_2 fed (0.7 and 1.7 SLPM, 1 bar_g) at 50 mA cm^{-2} for a) H^+ catalyst layer resistance. b) H^+ membrane resistance. c) O_2 diffusion resistance. d) ORR resistance. Cathode: 1.31 ± 0.05 $mg_{Fe\text{-}N\text{-}C}$ cm^{-2} TAP 900@Fe900 on Sigracet BC29. Anode: 0.2 mg_{Pt} cm^{-2} on Sigracet 22BB, with Nafion® 212 membrane.

improving O_2 transport in the ionomer. It could also arise due to the shifting primary O_2 reduction reaction zone in the Fe-N-C catalyst layer away from the membrane/Fe-N-C interface and toward the O_2 supply. This is supported by the results for H^+ transport resistance in the catalyst layer at I/C = 2.1, where ionomer was insufficient for H^+ supply (Figures 5a and S23a, Supporting Information).

The ORR resistance at 50 and 100 mA cm^{-2} is presented in Figures 5d and S24d (Supporting Information), respectively, and normalized results in Figure S22 (Supporting Information). The ORR resistance is affected by contributions of TOF, EASD, H^+ and O_2 transport resistances, as well as electronic conductivity and cell voltage (applied overpotential). The increase in ORR resistance at I/C = 2.1 is likely dominated by the increase in the H^+ transport resistance in the catalyst layer and membrane, and the decrease in TOF (Figures 5c and S24c, Supporting Information). For I/C ≥ 3.5 the H^+ catalyst layer and membrane resistance and O_2 diffusion resistance do not significantly increase (and in some cases decrease). Therefore, these processes can be excluded from the cause of the increased ORR resistance over the AST protocol. Moreover, as the AST progresses the cell voltage required to reach 50 and 100 mA cm^{-2} decreases, equivalent to an increase in the applied overpotential for O_2 reduction, to compensate for the loss of active sites and decrease in TOF.

Meanwhile, the electronic conductivity of the TAP 900@Fe900 layer over the AST decreases, as supported by the increasing R_u values over the AST (Table S2, Supporting Information), obtained from N_2-H_2 Nyquist plots (Figures S18–S21, Supporting Information), with the decrease likely caused by carbon oxidation (Figures 3 and S13, Supporting Information). The correlation between TOF and EASD with ORR resistance is presented in **Figures 6** and S25 (Supporting Information). From the DRT analysis we can conclude that the minor changes in H^+ and O_2 supply over the AST for I/C ≥ 3.5 demonstrate that the PEMFC degradation at high cell voltage (low current density) is caused by decreases in kinetics (EASD and TOF) and increased ohmic losses (electronic conductivity).

In this work AST cycling was stopped after only 1000 cycles due to the near complete loss of current density at relative PEMFC operating cell voltages (0.75 V, Figure 2). If AST cycling was continued it is expected that H^+ transport resistance from ionomer and membrane degradation would play a more significant role,[63] due to dissolved Fe replacement with H^+ in the ionomer, and hydroxyl radical attack from Fenton's reactions with H_2O_2.[66–68] Additionally, while the decay in the number of EASD would be expected to reduce, due to remaining sites being less active but more stable,[48] sites could still be loss via carbon corrosion. Carbon corrosion would eventually lead to reduced electronic conductivity and collapsed electrode structure from electrode thinning.[63]

3. Conclusions

A porous Fe-N-C in PEMFC with I/C = 2.1, 3.5, 4.2 and 4.9 was tested over an AST protocol. Significant Fe particle and FeN_x dissolution is confirmed over the 1000 AST cycles by comparing pristine and *post-mortem* STEM and EDXS. FeN_x active sites also suffer from reducing TOF arising from carbon oxidation (Raman and STEM-EDXS). Over the first 200 AST cycles, increased I/C caused increased EASD and rate of EASD loss, but a reduced

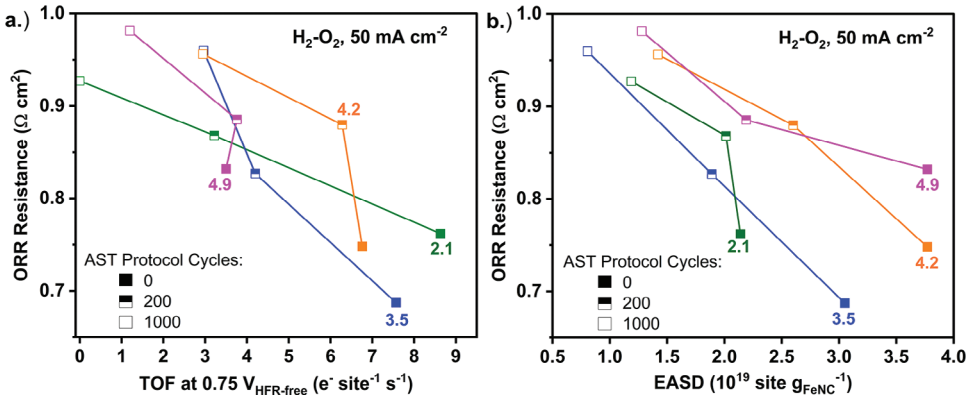

Figure 6. DRT derived ORR resistance at 50 mA cm^{-2} versus. a) TOF at 0.75 $V_{HFR-free}$ and b) EASD. TOF_{FTacV} and $EASD_{FTacV}$ are used for I/C ≤ 3.5, while TOF_{CV} and $EASD_{CV}$ is used for I/C = 4.9.

rate of TOF decay. Additionally, the initially lower S-number (after 200 AST cycles) with increasing I/C indicates active but unstable FeN_x active sites are located within the pores which are accessed by the ionomer at increased I/C ratios. After the 1000 AST cycles the I/C did not significantly impact on the S-number and TOF. PEMFC degradation was mainly related to kinetic losses as there was no significant increases in resistances to electrochemical processes over the AST protocol. This is proven by the correlation between TOF and EASD with ORR resistance derived from DRT.

4. Experimental Section

Synthesis: The Fe-N-C, denoted herein as TAP 900@Fe900, was synthesized according to our previously reported protocol,[70,71] which was also described in the Supporting Information. The difference between TAP 900@Fe and TAP 900@Fe900 was clarified here. TAP 900@Fe refer to samples were 2,4,6-Triaminopyrimidine was pyrolyzed (under N_2) to 900 °C (5 °C min^{-1}) for 1 h with Mg salt ($MgCl_2{\cdot}6H_2O$) in a 1:8 weight ratio and subsequently acid washed in 2 M HCl overnight. The filtered and dried sample was loaded with Fe by methanol reflux (90 °C) for 24 h and subsequently washed with 0.5 M H_2SO_4 overnight. The dried sample was termed TAP 900@Fe, which was previously thoroughly characterized and studied for Fe dissolution.[30,70] The reductive pyrolysis of TAP 900@Fe under 5% H_2/Ar at 25 °C min^{-1} up to 900 °C (1 h hold before natural cooling) led to TAP 900@Fe900.

Characterization: *Catalyst Characterization*: Measurement details for Raman spectroscopy, high-angle annular dark field scanning transmission electron microscopy (HAADF-STEM), scanning electron microscopy (SEM), transmission electron microscopy (TEM) and EDXS could be found in the Supporting Information.

Fuel Cell Testing: Electrodes were prepared according to our previous work.[71] Precious-metal free tools were used during cathode fabrication. Inks were prepared at a concentration of 2 mg_{FeNC} mL^{-1} with a ratio of 1:1 of isopropanol:water with Nafion solution (D2021 (1100 equivalent weight), Ion Power) added to achieve I/C of 2.1, 3.5, 4.2, 4.9 (wt. ratio). In terms of Nafion wt.% these values are equivalent to 68, 78, 81 and 83 wt.%. Previously, I/C = 0.7 and 1.4 were tested for initial performance in PEMFC;[71] however, their very poor initial performance did not warrant stability testing.

The mixture was placed in an ice-cooled bath sonicator (45 kHz, 50 W ultrasonic cleaner, MRC) for 1 h and then left stirring for 12–16 h. The cathode ink was then automatically spray-coated (Sono-Tek ExactaCoat, 48 kHz nozzle, 1.3 W) at a rate of 0.15 mL min^{-1} with an offset serpentine spray pattern on a 5 cm^2 gas diffusion layer (Sigracet BC29, SGL Group) while heated at 95 °C on a vacuum plate. Air shaping pressure was 0.3 psi. The gas diffusion layer was weighed pre and post cathode catalyst spraying to determine the cathode catalyst loading (1.35 ± 0.03 $mg_{Fe\text{-}N\text{-}C}$ cm^{-2}). Next, 0.2 mg cm^{-2} of Nafion solution (1 mg Nafion per mL IPA) was sprayed on the top of the cathode Fe-N-C. The 5 cm^2 electrode was then cut into 1 cm^2 pieces.

The anode was 0.2 mg_{Pt} cm^{-2} on Sigracet 22BB (Fuel Cells Etc) and the membrane was Nafion 212 (Ion Power). The anode, N212 membrane and cathode were hot pressed (Auto Series, Carver) at 125 °C for 5 min at 1814 kg. MEA gaskets thickness was selected for 20%–30% compression on GDL (anode gasket = 170 µm, cathode gasket = 220 µm). The PEMFC bolts were tightened to a torque of 4.5 N m. The cell was heated to 80 °C and humidified gases were first heated to 60 °C and then 80 °C, with gases flowing for 20 min to hydrate the Nafion 212 membrane.

PEMFC testing was measured on a Scribner 850e (Scribner Associates Inc.). Polarization curves were recorded under H_2-O_2 (H_2 and O_2 99.999%, MAXIMA) with 1 bar_g back pressure, 100% relative humidity, 80 °C cell and gas temperature and 0.7 and 1.7 standard L min^{-1} (SLPM) to the anode and cathode. Polarization curves were measured in 50 mV increments from open circuit potential to 0.2 V and back to open circuit potential. Cyclic voltammetry, under N_2-H_2 (cathode-anode, N_2 99.999%, MAXIMA) with 0.3 SLPM at both anode and cathode, was measured at 50 mV s^{-1} between 1.0–0.1 V with 10 scans to ensure a stable electrochemical response.

The whole fuel cell AST protocol was summarized in Figure S1 and Table S1 (Supporting Information). The AST cycling mimics the standardized protocol established by Zelenay and coworkers.[36] It should be noted that in this work, 0 AST cycles refers to point after the two polarization curves and 20 min 0.4 V hold (H_2-O_2) and before the 200 AST cycles (step 7 in Table S1, Supporting Information).

Fourier Transformed Alternating Current Voltammetry: The measurements followed a previously reported methods.[55,57,71] Fourier Transformed alternating current voltammetry was conducted using a Biologic SP-300 potentiostat. Cell conditions were the same as above under H_2-N_2. Initial voltage, E_i, was 0.55 V; final voltage, E_f, was 0.95 V; sine wave frequency, f, of 0.119 Hz; direct current scan rate of 0.476 mV s^{-1}; amplitude of sine wave, ΔE, of 130 mV; and time step for data acquisition, dt, of 0.8 ms.

Modelling was conducted on MATLAB, with the code provided on Github (https://github.com/Snitkoff-Sol). Inputs and outputs of FTacV were detailed in Table S2 (Supporting Information). Further details on the FTacV simulation could be found in previous works.[55–57]

Distribution of Relaxation Times: Electrochemical impendence spectroscopy (EIS) was measured with a Biologic SP-300 between 200 000–0.1 kHz with 20 points per decade and perturbation amplitude of 10 mV. Before each EIS measurement the cell was stabilized at 0.3 V for 30 s. Flow rates and PEMFC conditions in EIS were identical to polarization and cyclic

voltammetry. All EIS measurements were validated for linearity, causality, and stability by the Kramers-Kronig relations using the LIN-KK software developed by Ivers-Tiffée et al.,[78] where the residuals remained below 1%, confirming the validity of the EIS results. DRT analysis was conducted using the Matlab DRTTools software developed by Ciucci and Chen.[79] A Gaussian discretization method was applied, excluding inductive data due to the DRT method's inherent limitations in handling inductive processes. A second order regularization derivative was chosen for the analysis to minimize noise in the DRT solution. The regularization parameter (lambda) was set to 10^{-3} based on the work by Heinzmann et al.[77] Lower lambda values may introduce false peaks due to excessive sensitivity, while higher values may eliminate real peaks due to insufficient sensitivity. The resistance of the processes was determined by integrating the area under the corresponding peaks.

The geometric electrochemical active site density ($EASD_{geo}$) from Fe^{III}/Fe^{II} redox was calculated on the following Equation (1):

$$EASD_{geo} = \frac{Q_{Fe}}{F} \tag{1}$$

where Q_{Fe} is the Fe^{III}/Fe^{II} redox charge (C cm^{-2}) and F is Faraday's constant (96485 C mol^{-1}).

The gravimetric electrochemical active site density ($EASD_{mass}$) can then simply be determined from Equation (2):

$$EASD_{mass} = \frac{EASD_{geo} \times N_A}{L_{FeNC}} \tag{2}$$

where N_A is Avogadro's constant (6.023×10^{23} mol^{-1}) and L_{FeNC} represents the Fe-N-C catalyst loading (1.35 ± 0.03 mg_{FeNC} cm^{-2}).

TOF values in PEMFC at 0.75 $V_{HFR\text{-}free}$ were based on Equation (3), where HFR is the high frequency resistance (see Equation (5)).

$$TOF = \frac{i_{geo}}{e^- \times EASD_{geo}} \tag{3}$$

where i_{geo} is the geometric current density (mA cm^{-2}) at 0.75 $V_{HFR\text{-}free}$ and e^- is the charge of an electron (1.602×10^{-19} C).

The active site stability number can be calculated based on the charge passed over the AST and change in EASD in Equation (4):

$$S - number = \frac{Q_{AST}}{F \times \Delta EASD_{mol}} \tag{4}$$

where S-number is the stability number (-), Q_{AST} is the charge passed over the AST (C) and $\Delta EASD_{mol}$ is the change in EASD over the AST (mol).

HFR corrected cell voltage ($E_{HFR\text{-}free}$) is applied via Equation (5):

$$E_{HFR-free} = E_{cell} - \left(i_{geo} \times HFR\right) \tag{5}$$

where E_{cell} is the cell voltage (V).

The impedance can be described by Equation (6):

$$Z\ (f) = R_\infty + \int_{-\infty}^{\infty} \frac{\gamma\ (\ln \tau)}{1 + i2\pi f \tau} d \ln \tau \tag{6}$$

where Z is the impedance, f is the frequency, R_∞ is the high-frequency resistance, τ is the relaxation time, and $\gamma(\ln \tau)$ is the DRT function.

Supporting Information

Supporting Information is available from the Wiley Online Library or from the author.

Acknowledgements

The authors acknowledge financial support from the Engineering and Physical Sciences Research Council (EPSRC) (EP/W031019/1, EP/S023259/1, and EP/V001914/1), the European Research Council (ERC) under the European Union's Horizon 2020 research and innovation programme (grant agreement no. 866402 and no. 715502, EvoluTEM). A. P. thanks the EPSRC Centre for Doctoral Training in the Advanced Characterization of Materials (grant number EP/L015277/1), EPSRC Doctoral Prize Fellowship (EP/W524323/1) and the British/Israel Council/Wohl Clean Growth Alliance Foundation for funding. J. B. acknowledges financial support from Imperial College London through the Imperial College Research Fellowship. Electron microscopy access was supported by the Henry Royce Institute for Advanced Materials, funded through EPSRC grants EP/R00661X/1, EP/S019367/1, EP/P025021/1 and EP/P025498/1. R.Z.S.-S. thanks the Israeli Ministry of Energy for his fellowship. L. E. would like to thank the Israel Science Foundation and the Israeli Ministry of Energy for their financial support. This work was done in the Hydrogen Technologies (H2Tech) labs in the framework of the Israel National Institute for Energy Storage (INIES).

Conflict of Interest

The authors declare no conflict of interest.

Author Contributions

A.P. wrote the initial draft and led the investigation. A.P. synthesized the material and performed PEMFC testing. Y.P. performed DRT analysis and SEM measurements. A.P. and R. Z.S.-S. performed FTacV analysis. R.C. measured HAADF-STEM and EDXS. J.B. took part in the conceptualization of the material synthesis. L.D. measured SEM, TEM and EDXS. S.J. H., M.-M. T., i.e., L.S., and L.E. took part in the conceptualization of the work, analysis of the results, project supervision, and funded the project and resources. All authors contributed to reviewing and editing the manuscript.

Data Availability Statement

Data sharing is not applicable to this article as no new data were created or analyzed in this study.

Keywords

distribution relaxation times, Fourier transformed alternating current voltammetry, ionomer, PEMFC, single atom catalyst

Received: August 29, 2024
Revised: November 5, 2024
Published online:

[1] H. A. Gasteiger, S. S. Kocha, B. Sompalli, F. T. Wagner, *Appl. Catal. B Environ.* **2005**, *56*, 9.
[2] S. T. Thompson, D. Papageorgopoulos, *Nat. Catal.* **2019**, *2*, 558.
[3] A. Pedersen, J. Pandya, G. Leonzio, A. Serov, A. Bernardi, I. Stephens, M.-M. Titirici, C. Petit, B. Chachuat, *Green Chem.* **2023**, *25*, 10458.
[4] S. Liu, C. Li, M. J. Zachman, Y. Zeng, H. Yu, B. Li, M. Wang, J. Braaten, J. Liu, H. M. Meyer, M. Lucero, A. J. Kropf, E. E. Alp, Q. Gong, Q. Shi, Z. Feng, H. Xu, G. Wang, D. J. Myers, J. Xie, D. A. Cullen, S. Litster, G. Wu, *Nat. Energy* **2022**, *7*, 652.

[5] Y. Zeng, C. Li, B. Li, J. Liang, M. J. Zachman, D. A. Cullen, R. P. Hermann, E. E. Alp, B. Lavina, S. Karakalos, M. Lucero, B. Zhang, M. Wang, Z. Feng, G. Wang, J. Xie, D. J. Myers, J.-P. Dodelet, G. Wu, *Nat. Catal.* **2023**, *6*, 1215.
[6] O. E. Efficiency, R. Energy, *Development, and Demonstration Plan: 3.4 Fuel Cells*, US DOE, Washington **2016**.
[7] K. Kumar, L. Dubau, F. Jaouen, F. Maillard, *Chem. Rev.* **2023**, *123*, 9265.
[8] J. Herranz, F. Jaouen, M. Lefèvre, U. I. Kramm, E. Proietti, J. P. Dodelet, P. Bogdanoff, S. Fiechter, I. Abs-Wurmbach, P. Bertrand, T. M. Arruda, S. Mukerjee, *J. Phys. Chem. C* **2011**, *115*, 16087.
[9] X. Xie, C. He, B. Li, Y. He, D. A. Cullen, E. C. Wegener, A. J. Kropf, U. Martinez, Y. Cheng, M. H. Engelhard, M. E. Bowden, M. Song, T. Lemmon, X. S. Li, Z. Nie, J. Liu, D. J. Myers, P. Zelenay, G. Wang, G. Wu, V. Ramani, Y. Shao, *Nat. Catal.* **2020**, *3*, 1044.
[10] C. H. Choi, C. Baldizzone, J.-P. Grote, A. K. Schuppert, F. Jaouen, K. J. J. Mayrhofer, *Angew. Chem., Int. Ed.* **2015**, *54*, 12753.
[11] X. Tan, H. A. Tahini, S. C. Smith, *J. Mater. Chem. A* **2021**, *9*, 8721.
[12] A. Morankar, P. Atanassov, J. Greeley, *ChemPhysChem* **2024**, *25*, 202400199.
[13] S. T. Putnam, J. Rodríguez-López, *Chem. Sci.* **2024**, *15*, 10036.
[14] C. H. Choi, H. K. Lim, M. W. Chung, G. Chon, N. Ranjbar Sahraie, A. Altin, M. T. Sougrati, L. Stievano, H. S. Oh, E. S. Park, F. Luo, P. Strasser, G. Dražić, K. J. J. Mayrhofer, H. Kim, F. Jaouen, *Energy Environ. Sci.* **2018**, *11*, 3176.
[15] V. Gridin, N. Segura-Salas, V. A. Saveleva, P. Theis, S. Haller, C. C. Ribeiro, K. Hofmann, R. Stark, U. I. Kramm, *ACS Catal.* **2024**, *14*, 10951.
[16] C.-Y. Qiu, L. Wan, Y.-C. Wang, M. Rauf, Y.-H. Hong, J. Yuan, Z.-Y. Zhou, S.-G. Sun, *Chin. J. Catal.* **2022**, *43*, 1918.
[17] S. Ünsal, R. Girod, C. Appel, D. Karpov, M. Mermoux, F. Maillard, V. A. Saveleva, V. Tileli, T. J. Schmidt, J. Herranz, *J. Am. Chem. Soc.* **2023**, *145*, 7845.
[18] G. Zhang, R. Chenitz, M. Lefèvre, S. Sun, J.-P. Dodelet, *Nano Energy* **2016**, *29*, 111.
[19] L. Yang, N. Larouche, R. Chenitz, G. Zhang, M. Lefèvre, J.-P. Dodelet, *Electrochim. Acta* **2015**, *159*, 184.
[20] M. Primbs, Y. Sun, A. Roy, D. Malko, A. Mehmood, M.-T. Sougrati, P.-Y. Blanchard, G. Granozzi, T. Kosmala, G. Daniel, P. Atanassov, J. Sharman, C. Durante, A. Kucernak, D. Jones, F. Jaouen, P. Strasser, *Energy Environ. Sci.* **2020**, *13*, 2480.
[21] E. F. Holby, P. Zelenay, *Nano Energy* **2016**, *29*, 54.
[22] F. Jaouen, M. Lefèvre, J.-P. Dodelet, M. Cai, *J. Phys. Chem. B* **2006**, *110*, 5553.
[23] M. Lefèvre, E. Proietti, F. Jaouen, J. P. Dodelet, *ScienceScience* **2009**, *324*, 71.
[24] Y.-C. Wang, W. Huang, L.-Y. Wan, J. Yang, R.-J. Xie, Y.-P. Zheng, Y.-Z. Tan, Y.-S. Wang, K. Zaghib, L.-R. Zheng, S.-H. Sun, Z.-Y. Zhou, S.-G. Sun, *Sci. Adv.* **2022**, *8*, eadd8873.
[25] J.-Y. Choi, L. Yang, T. Kishimoto, X. Fu, S. Ye, Z. Chen, D. Banham, *Energy Environ. Sci.* **2017**, *10*, 296.
[26] R. Chenitz, U. I. Kramm, M. Lefèvre, V. Glibin, G. Zhang, S. Sun, J.-P. Dodelet, *Energy Environ. Sci.* **2018**, *11*, 365.
[27] L. Castanheira, L. Dubau, M. Mermoux, G. Berthomé, N. Caqué, E. Rossinot, M. Chatenet, F. Maillard, *ACS Catal.* **2014**, *4*, 2258.
[28] L. Castanheira, W. O. Silva, F. H. B. Lima, A. Crisci, L. Dubau, F. Maillard, *ACS Catal.* **2015**, *5*, 2184.
[29] K. Kumar, T. Asset, X. Li, Y. Liu, X. Yan, Y. Chen, M. Mermoux, X. Pan, P. Atanassov, F. Maillard, L. Dubau, *ACS Catal.* **2021**, *11*, 484.
[30] A. Pedersen, K. Kumar, Y.-P. Ku, V. Martin, L. Dubau, K. T. Santos, J. Barrio, V. A. Saveleva, P. Glatzel, V. K. Paidi, X. Li, A. Hutzler, M.-M. Titirici, A. Bonnefont, S. Cherevko, I. E. L. Stephens, F. Maillard, *Energy Environ. Sci.* **2024**, *17*, 6323.
[31] K. Kumar, P. Gairola, M. Lions, N. Ranjbar-Sahraie, M. Mermoux, L. Dubau, A. Zitolo, F. Jaouen, F. Maillard, *ACS Catal.* **2018**, *8*, 11264.
[32] D. E. Beltrán, Y. Zeng, G. Wu, X. Li, S. Litster, *Electrochim. Acta* **2024**, *503*, 144837.
[33] K. Kumar, L. Dubau, M. Mermoux, J. Li, A. Zitolo, J. Nelayah, F. Jaouen, F. Maillard, *Angew. Chem., Int. Ed.* **2020**, *59*, 3235.
[34] L. Osmieri, D. A. Cullen, H. T. Chung, R. K. Ahluwalia, K. C. Neyerlin, *Nano Energy* **2020**, *78*, 105209.
[35] D. Banham, T. Kishimoto, T. Sato, Y. Kobayashi, K. Narizuka, J. Ichi Ozaki, Y. Zhou, E. Marquez, K. Bai, S. Ye, *J. Power Sources* **2017**, *344*, 39.
[36] H. Zhang, L. Osmieri, J. H. Park, H. T. Chung, D. A. Cullen, K. C. Neyerlin, D. J. Myers, P. Zelenay, *Nat. Catal.* **2022**, *5*, 455.
[37] V. A. Saveleva, K. Kumar, P. Theis, N. S. Salas, U. I. Kramm, F. Jaouen, F. Maillard, P. Glatzel, *ACS Appl. Energy Mater.* **2023**, *6*, 611.
[38] G. Bae, M. M. Kim, M. H. Han, J. Cho, D. H. Kim, M.-T. Sougrati, J. Kim, K.-S. Lee, S. H. Joo, W. A. Goddard, H.-S. Oh, H. Kim, F. Jaouen, C. H. Choi, *Nat. Catal.* **2023**, *6*, 1140.
[39] G. Bae, H. C. Kwon, M. H. Han, H.-S. Oh, F. Jaouen, C. H. Choi, *ACS Catal.* **2024**, *14*, 8184.
[40] F. Luo, C. H. Choi, M. J. M. Primbs, W. Ju, S. Li, N. D. Leonard, A. Thomas, F. Jaouen, P. Strasser, *ACS Catal.* **2019**, *9*, 4841.
[41] D. Menga, A. G. Buzanich, F. Wagner, T.-P. Fellinger, *Angew. Chem., Int. Ed.* **2022**, *61*, 202207089.
[42] D. Malko, A. Kucernak, T. Lopes, *Nat. Commun.* **2016**, *7*, 13285.
[43] A. Mehmood, M. Gong, F. Jaouen, A. Roy, A. Zitolo, A. Khan, M. Sougrati, M. Primbs, A. M. Bonastre, D. Fongalland, G. Drazic, P. Strasser, A. Kucernak, *Nat. Catal.* **2022**, *5*, 311.
[44] M. Gong, A. Mehmood, B. Ali, K.-W. Nam, A. Kucernak, *ACS Catal.* **2023**, *13*, 6661.
[45] D. H. Kim, S. Ringe, H. Kim, S. Kim, B. Kim, G. Bae, H.-S. Oh, F. Jaouen, W. Kim, H. Kim, C. H. Choi, *Nat. Commun.* **2021**, *12*, 1856.
[46] G. Bae, H. Kim, H. Choi, P. Jeong, D. H. Kim, H. C. Kwon, K.-S. Lee, M. Choi, H.-S. Oh, F. Jaouen, C. H. Choi, *JACS Au* **2021**, *1*, 586.
[47] Q. Jia, N. Ramaswamy, H. Hafiz, U. Tylus, K. Strickland, G. Wu, B. Barbiellini, A. Bansil, E. F. Holby, P. Zelenay, S. Mukerjee, *ACS Nano* **2015**, *9*, 12496.
[48] J. Li, M. T. Sougrati, A. Zitolo, J. M. Ablett, I. C. Oğuz, T. Mineva, I. Matanovic, P. Atanassov, Y. Huang, I. Zenyuk, A. Di Cicco, K. Kumar, L. Dubau, F. Maillard, G. Dražić, F. Jaouen, *Nat. Catal.* **2021**, *4*, 10.
[49] L. Osmieri, R. K. Ahluwalia, X. Wang, H. T. Chung, X. Yin, A. J. Kropf, J. Park, D. A. Cullen, K. L. More, P. Zelenay, D. J. Myers, K. C. Neyerlin, *Appl. Catal. B Environ.* **2019**, *257*, 117929.
[50] X. Wang, M. Ferrandon, J. H. Park, J.-J. Shen, A. J. Kropf, H. Zhang, P. Zelenay, D. J. Myers, *Electrochim. Acta* **2023**, *443*, 141934.
[51] K. Kinoshita, J. A. S. Bett, *CarbonCarbon* **1973**, *11*, 403.
[52] Q. Meyer, S. Liu, Y. Li, C. Zhao, *J. Power Sources* **2022**, *533*, 231058.
[53] N. G. Baranska, B. Jones, M. R. Dowsett, C. Rhodes, D. M. Elton, J. Zhang, A. M. Bond, D. Gavaghan, H. O. Lloyd-Laney, A. Parkin, *ACS Meas. Sci.* **2024**, *4*, 418.
[54] A. M. Bond, N. W. Duffy, D. M. Elton, B. D. Fleming, *Anal. Chem.* **2009**, *81*, 8801.
[55] R. Z. Snitkoff-Sol, A. Friedman, H. C. Honig, Y. Yurko, A. Kozhushner, M. J. Zachman, P. Zelenay, A. M. Bond, L. Elbaz, *Nat. Catal.* **2022**, *5*, 163.
[56] A. Friedman, R. Z. Snitkoff-Sol, H. C. Honig, L. Elbaz, *Electrochim. Acta* **2023**, *463*, 142865.
[57] R. Z. Snitkoff-Sol, O. Rimon, A. M. Bond, L. Elbaz, *Nat. Catal.* **2024**, *7*, 139.
[58] R. Z. Snitkoff-Sol, A. M. Bond, L. Elbaz, *ACS Catal.* **2024**, *14*, 7576.
[59] R. Z. Snitkoff-Sol, L. Elbaz, *J. Solid State Electrochem.* **2022**, *26*, 1839.
[60] S. Geiger, O. Kasian, M. Ledendecker, E. Pizzutilo, A. M. Mingers, W. T. Fu, O. Diaz-Morales, Z. Li, T. Oellers, L. Fruchter, A. Ludwig, K. J. J. Mayrhofer, M. T. M. Koper, S. Cherevko, *Nat. Catal.* **2018**, *1*, 508.

[61] A. Pedersen, A. Bagger, J. Barrio, F. Maillard, I. Stephens, M.-M. Titirici, *J. Mater. Chem. A* **2023**, *11*, 23211.
[62] Y.-P. Ku, K. Ehelebe, A. Hutzler, M. Bierling, T. Böhm, A. Zitolo, M. Vorokhta, N. Bibent, F. D. Speck, D. Seeberger, I. Khalakhan, K. J. J. Mayrhofer, S. Thiele, F. Jaouen, S. Cherevko, *J. Am. Chem. Soc.* **2022**, *144*, 9753.
[63] S. Liu, Q. Meyer, C. Jia, S. Wang, C. Rong, Y. Nie, C. Zhao, *Energy Environ. Sci.* **2023**, *16*, 3792.
[64] Y. Yurko, L. Elbaz, *Electrochim. Acta* **2023**, *463*, 142877.
[65] A. Maradesa, B. Py, J. Huang, Y. Lu, P. Iurilli, A. Mrozinski, H. M. Law, Y. Wang, Z. Wang, J. Li, S. Xu, Q. Meyer, J. Liu, C. Brivio, A. Gavrilyuk, K. Kobayashi, A. Bertei, N. J. Williams, C. Zhao, M. Danzer, M. Zic, P. Wu, V. Yrjänä, S. Pereverzyev, Y. Chen, A. Weber, S. V. Kalinin, J. P. Schmidt, Y. Tsur, et al., *Joule* **2024**, *8*, 1958.
[66] A. Pozio, R. F. Silva, M. De Francesco, L. Giorgi, *Electrochim. Acta* **2003**, *48*, 1543.
[67] V. Goellner, V. Armel, A. Zitolo, E. Fonda, F. Jaouen, *J. Electrochem. Soc.* **2015**, *162*, H403.
[68] C. H. Choi, C. Baldizzone, G. Polymeros, E. Pizzutilo, O. Kasian, A. K. Schuppert, N. Ranjbar Sahraie, M.-T. Sougrati, K. J. J. Mayrhofer, F. Jaouen, *ACS Catal.* **2016**, *6*, 3136.
[69] K. Artyushkova, M. J. Workman, I. Matanovic, M. J. Dzara, C. Ngo, S. Pylypenko, A. Serov, P. Atanassov, *ACS Appl. Energy Mater.* **2018**, *1*, 68.
[70] J. Barrio, A. Pedersen, S. Ch. Sarma, A. Bagger, M. Gong, S. Favero, C. Zhao, R. Garcia-Serres, A. Y. Li, Q. Zhang, F. Jaouen, F. Maillard, A. Kucernak, I. E. L. Stephens, M. Titirici, *Adv. Mater.* **2023**, *35*, 2211022.
[71] A. Pedersen, R. Z. Snitkoff-Sol, Y. Presman, J. Barrio, R. Cai, T. Suter, G. Yang, S. J. Haigh, D. Brett, R. Jervis, M.-M. Titirici, I. E. L. Stephens, L. Elbaz, *J. Power Sources* **2024**, *609*, 234683.
[72] V. G. Chandrashekhar, T. Senthamarai, R. G. Kadam, O. Malina, J. Kašlík, R. Zbořil, M. B. Gawande, R. V. Jagadeesh, M. Beller, *Nat. Catal.* **2022**, *5*, 20.
[73] K. T. Santos, K. Kumar, L. Dubau, H. Ge, S. Berthon-Fabry, C. S. A. Vasconcellos, F. H. B. Lima, T. Asset, P. Atanassov, V. A. Saveleva, P. Glatzel, X. Li, F. Jaouen, F. Maillard, *J. Power Sources* **2023**, *564*, 232829.
[74] Y.-S. Li, D. Menga, H. A. Gasteiger, B. Suthar, *J. Electrochem. Soc.* **2023**, *170*, 094503.
[75] J. Liu, M. R. Talarposhti, T. Asset, D. C. Sabarirajan, D. Y. Parkinson, P. Atanassov, I. V. Zenyuk, *ACS Appl. Energy Mater.* **2019**, *2*, 3542.
[76] J. Durst, M. Chatenet, F. Maillard, *Phys. Chem. Chem. Phys.* **2012**, *14*, 13000.
[77] M. Heinzmann, A. Weber, E. Ivers-Tiffée, *J. Power Sources* **2018**, *402*, 24.
[78] M. Schönleber, D. Klotz, E. Ivers-Tiffée, *Electrochim. Acta* **2014**, *131*, 20.
[79] F. Ciucci, C. Chen, *Electrochim. Acta* **2015**, *167*, 439.